Surface Molecular Functionalization of Unusual Phase Metal Nanomaterials for Highly Efficient Electrochemical Carbon Dioxide Reduction under Industry-Relevant Current Density

Juan Wang, Jinli Yu, Mingzi Sun, Lingwen Liao, Qinghua Zhang, Li Zhai, Xichen Zhou, Lujiang Li, Gang Wang, Fanqi Meng, Dong Shen, Zijian Li, Haibo Bao, Yunhao Wang, Jingwen Zhou, Ye Chen, Wenxin Niu, Bolong Huang, Lin Gu,* Chun-Sing Lee and Zhanxi Fan**

J. Wang, J. Yu, Prof. L. Liao, L. Zhai, X. Zhou, L. Li, D. Shen, Z. Li, Y. Wang, J. Zhou, Prof. C.-S. Lee, Prof. Z. Fan
Department of Chemistry, City University of Hong Kong, Hong Kong, China.
E-mail: zhanxi.fan@cityu.edu.hk

J. Zhou, Prof. Z. Fan
Hong Kong Branch of National Precious Metals Material Engineering Research Center (NPMM), City University of Hong Kong, Hong Kong, China.

M. Sun, Prof. B. Huang
Department of Applied Biology and Chemical Technology, The Hong Kong Polytechnic University, Hung Hom, Kowloon, Hong Kong SAR, China.
E-mail: bhuang@polyu.edu.hk

Prof. Q. Zhang, F. Meng, Prof. L. Gu
Institute of Physics, Beijing National Laboratory for Condensed Matter Physics, Chinese Academy of Sciences, Beijing 100190, China.
E-mail: l.gu@iphy.ac.cn

G. Wang, Prof. Y. Chen
Department of Chemistry, The Chinese University of Hong Kong, Hong Kong, China.

H. Bao, Prof. W. Niu
State Key Laboratory of Electroanalytical Chemistry, Changchun Institute of Applied Chemistry, Chinese Academy of Sciences, Changchun 130021, China.

Prof. C.-S. Lee
Center of Super-Diamond and Advanced Films (COSDAF), City University of Hong Kong, Hong Kong, China.

Prof. Z. Fan
City University of Hong Kong Shenzhen Research Institute, Shenzhen 518057, China.

Keywords: metal nanomaterials, unusual phase, surface molecular functionalization, electrocatalysis, carbon dioxide reduction reaction

Abstract

Electrochemical carbon dioxide reduction reaction (CO_2RR) provides a sustainable strategy to relieve global warming and achieve carbon neutral. However, practical application of CO_2RR is still limited by the poor selectivity and low current density. Here we first report the surface molecular functionalization of unusual phase metal nanomaterials for high-performance CO_2RR under industry-relevant current density. It was observed that 5-mercapto-1-methyltetrazole (MMT)-modified 4H/face-centered cubic (fcc) Au nanorods demonstrate greatly enhanced CO_2RR performance than original oleylamine (OAm)-capped 4H/fcc Au nanorods in both H-type cell and flow cell. Significantly, MMT-modified 4H/fcc Au nanorods deliver an excellent carbon monoxide selectivity of 95.6% under the industry-relevant current density of 200 mA cm^{-2}. Density functional theory calculations reveal distinct electronic modulations by surface ligands, in which MMT improves while OAm suppresses the surface electroactivity of 4H/fcc Au nanorods. Furthermore, this method can be extended to various MMT derivatives and conventional fcc Au nanostructures in boosting CO_2RR performance.

1. Introduction

The energy-efficient conversion of carbon dioxide (CO_2) has attracted worldwide attention as it holds huge potential to relieve global warming and achieve carbon neutral.[1-4] Among different CO_2 conversion technologies, electrochemical CO_2 reduction reaction (CO_2RR) offers a sustainable strategy to convert CO_2 into value-added chemicals and fuels.[5-8] To promote the practical applications of electrochemical CO_2RR, great research efforts, such as composition modulation,[9, 10] facet regulation,[11, 12] defect control,[13-16] strain adjustment[17, 18] and phase engineering[19-23] of catalysts, have been devoted to tune the reaction pathway and increase the selectivity of target products.[24] In particular, highly efficient and selective conversion of CO_2 into carbon monoxide (CO) is a promising way toward industrial application as CO can be easily separated and widely utilized as a feedstock to generate various high-value chemicals and fuels.[25, 26] Metal nanomaterials, especially gold (Au)[27-30] and silver (Ag),[31-33] are promising catalysts for the electrochemical reduction of CO_2 to CO. However, most metal catalysts still suffer from low activity and the volcano-type CO Faradaic efficiency (FE) as a function of applied potentials.

Very recently, surface modification of metal materials has emerged as a versatile strategy to improve the electrochemical CO_2RR performance.[34, 35] On the one hand, surface modification could fine tune the electronic structure,[36, 37] chemical state,[38, 39] composition[40, 41] and surface roughness[42, 43] of metal materials to boost the electrocatalytic CO_2RR activity. On the other hand, surface modification of metal materials could also enhance the CO_2RR selectivity by modulating the stability of intermediates and regulating the reaction pathways.[44, 45] To enhance the CO_2RR performance, surface modification has been applied to functionalize the surface of various metal materials, such as copper (Cu),[45-49], Au,[40, 44, 50] palladium (Pd),[36, 37, 51] and Ag.[43, 52, 53] Unfortunately, the crystal phase of all the aforementioned metal materials is constrained to conventional phase, which could greatly impede the practical application of

CO_2RR. Note that recent studies have indicated that unusual phase metal nanomaterials usually possess much higher intrinsic catalytic activity than their conventional phase counterparts.[54-60] Therefore, surface modification of unusual phase metal nanomaterials could be a promising approach to further facilitate the real application of CO_2RR.

Herein, for the first time, we report the surface molecular functionalization of unusual phase 4H/face-centered cubic (fcc) Au nanorods with 5-mercapto-1-methyltetrazole (MMT) for high-performance electrochemical CO_2RR under industry-relevant current density. The MMT-modified 4H/fcc Au nanorods (denoted as 4H/fcc Au-MMT) demonstrate significantly enhanced CO_2RR performance than the initial oleylamine (OAm)-capped 4H/fcc Au nanorods (denoted as 4H/fcc Au-OAm) in H-type cell and flow cell under a wide range of potentials and current densities, respectively. Density functional theory (DFT) calculations indicate that surface molecular functionalization of 4H/fcc Au nanorods with MMT could improve the electroactivity and reduce the energy barriers to guarantee efficient CO_2RR. This facile surface molecular functionalization strategy is applicable to not only a family of MMT derivatives but also conventional fcc Au nanostructures in improving the CO_2RR performance.

2. Results and discussion

The 4H/fcc Au-OAm were synthesized by our previously reported method with slight modification,[61] see "Methods" for details. As shown in Figure S1a, b, scanning electron microscopy (SEM) and transmission electron microscopy (TEM) images show that Au nanorods with diameters of 10-30 nm and lengths of 300-1000 nm were successfully synthesized. High-resolution TEM (HRTEM) image of a representative Au nanorod and the corresponding selected-area fast Fourier transform (FFT) patterns confirm the formation of unconventional 4H/fcc crystal phase heterostructure (Figure S1c-e). The X-ray diffraction (XRD) pattern of 4H/fcc Au-OAm also identifies two sets of diffraction peaks associated with

4H and fcc phases, respectively (Figure S2). Besides, the Fourier-transform infrared (FT-IR) spectrum of 4H/fcc Au-OAm suggests that their surfaces are capped by OAm (Figure S3).

The surface molecular functionalization of 4H/fcc Au nanorods was achieved through the ligand exchange method, as shown in **Figure 1**a. Typically, 4H/fcc Au-MMT were obtained by mixing the solution of 4H/fcc Au-OAm with MMT solution, followed by vortexing and stirring at ambient conditions (see "Methods" for details). After the ligand exchange, SEM and TEM images reveal that 4H/fcc Au-MMT possess identical morphology to the original 4H/fcc Au-OAm (Figure S4). Both "ABCB" and "ABC" characteristic stacking sequences along the close-packed directions can be observed in the aberration-corrected high-angle annular dark-field scanning TEM (HAADF-STEM) images (Figure 1b, c), indicating the existence of 4H/fcc crystal phase heterostructure after ligand exchange. The crystal phase heterostructure of 4H/fcc Au-MMT was further confirmed by the XRD pattern (Figure S5). In addition, the FT-IR spectrum of 4H/fcc Au-MMT exhibits the similar spectral features to that of pure MMT in the range of 1700−700 cm^{-1} (Figure S6), suggesting the successful molecular functionalization of 4H/fcc Au nanorods with MMT. The representative HAADF-STEM image and the corresponding STEM-energy dispersive X-ray spectroscopy (STEM-EDS) elemental mappings show the homogeneous distribution of Au, S and N elements on 4H/fcc Au-MMT (Figure 1d-f), indicating the uniform coating of MMT on 4H/fcc Au nanorods. The X-ray photoelectron spectroscopy (XPS) spectra confirm the metallic state of Au in both 4H/fcc Au-MMT and 4H/fcc Au-OAm (Figure S7).[62] Note that the Au 4f peaks of 4H/fcc Au-MMT slightly shift to the higher binding energy compared to that of 4H/fcc Au-OAm, which could be attributed to the strong interaction between Au atoms and thiol groups in MMT.[63] Owing to the spin–orbit splitting, the S 2p spectrum of 4H/fcc Au-MMT can be fitted into two sets of doublet peaks (Figure S8a). Two major peaks at 161.7 eV and 162.8 eV are associated with S $2p_{3/2}$ and S $2p_{1/2}$ spectra, indicating the formation of Au-S bonds.[64] The other two minor peaks (i.e., S $2p_{3/2}$

(163.4 eV) and S $2p_{1/2}$ (164.5 eV)) are assigned to S-C bonds.[63, 65] The N 1s spectrum of 4H/fcc Au-MMT also shows two peaks located at 399.5 eV and 400.3 eV (Figure S8b), which are attributed to the two kinds of nitrogen environment in MMT, i.e., N=N/N−N and N=C/N−C, respectively.[66] The aforementioned XPS results further corroborate the successful surface molecular functionalization of 4H/fcc Au nanorods with MMT.

By using the 4H/fcc Au nanorods as a model catalyst, we systematically investigated the effect of surface molecular functionalization on the catalytic performance of 4H/fcc Au nanorods towards the electrochemical CO_2RR. The catalytic activity of 4H/fcc Au-MMT and 4H/fcc Au-OAm were first evaluated in the H-type cell with 0.5 M $KHCO_3$ aqueous electrolyte. The obtained gaseous and liquid products of CO_2RR were analyzed through an on-line gas chromatography and characterized by the ^{1}H nuclear magnetic resonance (NMR) spectroscopy, respectively. As shown in **Figure 2**a, the linear sweep voltammetry (LSV) measurements revealed that 4H/fcc Au-MMT exhibit a much larger current density than the 4H/fcc Au-OAm. The 4H/fcc Au-MMT also delivers a much higher FE of CO than the 4H/fcc Au-OAm in a wide operating potential window (Figure 2b). In particular, the 4H/fcc Au-MMT demonstrates a FE_{CO} over 97.5% in the potential range of −0.5 V to −0.8 V (vs reversible hydrogen electrode (RHE)), suggesting the almost complete suppression of the competing hydrogen evolution reduction (HER) process (Figure S9a). In contrast, the 4H/fcc Au-OAm only shows the maximum FE_{CO} of 83.1% at −0.6 V (vs RHE). As a result, the 4H/fcc Au-MMT exhibits a much larger geometric CO partial current density (J_{CO}) than 4H/fcc Au-OAm over a wide potential range (Figure 2c). Significantly, the geometric J_{CO} of 4H/fcc Au-MMT reaches 14.5 mA cm^{-2} at −0.9 V (vs RHE), which is almost two times that of 4H/fcc Au-OAm. By normalizing the J_{CO} to the electrochemical active surface area (ECSA, Figure S10), the specific J_{CO} under different potentials was obtained (Figure 2d). The 4H/fcc Au-MMT also shows relatively higher specific activity than 4H/fcc Au-OAm, which suggests that 4H/fcc Au-MMT possesses larger intrinsic

catalytic activity than 4H/fcc Au-OAm. In addition, as shown in Figure S9b, formate ($HCOO^-$) is one of the main products at the applied potential of −0.4 V (vs RHE). In specific, the FE_{HCOO^-} of 4H/fcc Au-MMT is 42.7%, which is over two times that of 4H/fcc Au-OAm. Only trace amount of $HCOO^-$ was detected in the potential range of −0.5 V to −1.0 V (vs RHE) for both 4H/fcc Au-MMT and 4H/fcc Au-OAm. These results suggest that 4H/fcc Au-MMT possess much superior electrochemical CO_2RR performance than the 4H/fcc Au-OAm in the whole operating potential window of −0.4 V to −1.0 V (vs RHE).

To investigate the reaction kinetics, Tafel slope analysis was conducted by linearly fitting the plot of overpotential versus the logarithm of the absolute value of geometric J_{CO}. As shown in Figure 2e, 4H/fcc Au-MMT demonstrates a much smaller Tafel slope of 73.5 mV dec^{-1} than the 4H/fcc Au-OAm (86.7 mV dec^{-1}). The aforementioned Tafel slopes suggest that both Au electrocatalysts possess a common reaction mechanism: undergoing a fast one-electron transfer process to form $CO_2^{\bullet-}$, and followed by the combination of $CO_2^{\bullet-}$ and a proton to generate *COOH as the rate-determining step. The smaller Tafel slope of 4H/fcc Au-MMT indicates that they can deliver a higher charge transfer coefficient than 4H/fcc Au-OAm. Moreover, electrochemical impedance spectroscopy (EIS) measurements were also performed to further compare their charge transfer behaviors. As shown in the Nyquist plots (Figure 2f), the 4H/fcc Au-MMT show a lower charge transfer resistance (R_{ct}) of 54.22 Ω than the 4H/fcc Au-OAm (63 Ω), which suggests that the surface molecular functionalization of 4H/fcc Au nanorods with MMT can enhance the charge transfer to CO_2.

As a control experiment, the CO_2RR performance of pure MMT in H-type cell was also evaluated under the same testing condition with a loading amount of 200 μg cm^{-2} (Figure S11). The onset potential of MMT in CO_2RR is −0.57 V (vs RHE). It was observed that products are mainly H_2 and $HCOO^-$, together with a trace amount of CO (below 5 ppm). MMT exhibits the FE_{H2} over 80% and the FE_{HCOO^-} below 20% in the potential range of −0.6 V to −1.0 V (vs RHE).

These results suggest that MMT in the 4H/fcc Au-MMT is not the active site for the electrochemical reduction of CO_2 to CO.

The current density in H-type cell is usually restricted by the mass transfer limitation of CO_2 in aqueous media. In order to achieve efficient electroreduction of CO_2 to CO under the industry-relevant current density, CO_2RR performance of 4H/fcc Au-MMT and 4H/fcc Au-OAm was investigated under constant current densities with the flow cell, as shown in **Figure 3**a. To avoid the energy loss resulted from the reaction between CO_2 and KOH aqueous electrolyte, 1.0 M $KHCO_3$ was adopted as catholyte.[67-69] Firstly, the CO_2RR performance of two Au electrocatalysts was measured with the Au loading amount of 200 μg. CO and H_2 are the main products (Figures 3b and S12a), along with trace amount of $HCOO^-$ (Figure S12b). The 4H/fcc Au-MMT demonstrates much higher CO selectivity than the 4H/fcc Au-OAm under entire current density range of 10−200 mA cm^{-2}. In specific, the FE_{CO} of 4H/fcc Au-MMT could well maintain over 96.3% in a wide current density range of 25−100 mA cm^{-2} (Figure 3b). In contrast, the 4H/fcc Au-OAm just exhibits the FE_{CO} of over 80% in a narrow current density range of 10−50 mA cm^{-2}. As the current density increases above 50 mA cm^{-2}, the FE_{CO} of 4H/fcc Au-OAm decreases sharply, together with the greatly enhanced HER process (Figures 3b and S12a). Impressively, at the current density of 200 mA cm^{-2}, the FE_{CO} of 4H/fcc Au-MMT is still around 70%, while 4H/fcc Au-OAm mainly favors the competing HER process. To further optimize the CO_2RR performance of 4H/fcc Au-MMT, the Au loading amount of 4H/fcc Au-MMT was increased to 400 μg. Significantly, under this condition, the 4H/fcc Au-MMT demonstrates FE_{CO} of 95.6% at the current density of 200 mA cm^{-2}, and FE_{CO} over 95% in the wide current density range of 10−200 mA cm^{-2} (Figure 3b). These results suggest that the surface molecular functionalization of 4H/fcc Au nanorods with MMT can significantly enhance their CO_2RR performance under the industry-relevant current density.

The long-term durability test of 4H/fcc Au-MMT was performed at 50 mA cm^{-2} for CO_2RR

(Figure 3c). The FE_{CO} of 4H/fcc Au-MMT exhibits negligible decrease, and well maintains over 92.3% after the 12 h electrolysis. Simultaneously, the potential for 50 mA cm^{-2} remains stable at around −0.7 V (vs RHE) during this long-term stability measurement. TEM, HRTEM and EDS characterizations confirm that the structure and composition of 4H/fcc Au-MMT are well preserved after the durability test (Figure S13), suggesting that 4H/fcc Au-MMT possess excellent electrocatalytic stability. The CO_2RR performance of 4H/fcc Au-MMT in flow cell is much superior over those of previously reported Au electrocatalysts with neutral or quasi-neutral catholytes, and even better than those using strong alkaline catholytes (Figure 3d and Table S1).[28, 70-73]

DFT calculations were conducted to unravel the modulation effect of different ligands on 4H/fcc Au nanorod surface for the CO_2RR. The electronic distributions near the Fermi level (E_F) have been compared on both 4H/fcc Au-OAm and 4H/fcc Au-MMT (**Figure 4**a, b). For the synthesized 4H/fcc Au nanorods with OAm on the surface, both bonding and anti-bonding orbitals are mostly dominated by the surface OAm molecules. The electronic distributions on Au surface are not evident, indicating that OAm molecules are able to passivate the electroactivity of Au surface (Figure 4a). Meanwhile, the coverage of OAm also hinders the adsorption of reactants due to spatial barriers. In comparison, the evident activations of Au surface are observed by the adsorption of MMT molecules (Figure 4b). The strong *p-d* couplings between Au and the S sites of MMT molecule achieve the electron-rich feature of Au surface, which supports the high electroactivity for CO_2RR. These results indicate that different ligands display distinct electronic modulations for the Au surface.

To obtain more information on the electronic structures, we have demonstrated the projected partial density of states (PDOS) of the 4H/fcc Au-OAm and 4H/fcc Au-MMT (Figure 4c, d). For the 4H/fcc Au-MMT, Au-5*d* orbitals show a peak near E_V-2.42 eV with *d*-band center at E_V-3.48 eV (E_V = 0 eV). Meanwhile, the *s,p* orbitals of MMT molecules on the surface exhibit

a broad overlapping with surface Au (Figure 4c), supporting the activations of Au by the *p-d* couplings. In comparison, 4H/fcc Au-OAm display obviously different electronic structures (Figure 4d). With the large OAm molecules on the surface, Au-5*d* orbitals become much broader than that with MMT molecules. These modulations further lower the *d*-band center to E_V-4.72 eV, revealing the suppressed electroactivity. Interestingly, the *s,p* orbitals of OAm show the evident occupation near E_F rather than Au-5*d* orbitals. Such electronic structures confirm that the OAm molecules will significantly passivate the electroactivity of Au surface. Then the site-dependent PDOS of Au-5*d* orbitals are calculated to compare the electroactivity modulations by different ligands (Figure 4e, f). In 4H/fcc Au-MMT, Au-5*d* orbitals demonstrate the synchronic upshifting trend from the bulk to the surface in both 4H and fcc phases (Figure 4e). In particular, the Au sites near adsorbed MMT molecules show an even higher *d*-band center and the dominant peak of 5*d* bands, which further confirm the promotion effect by the MMT molecules. On the other side, the OAm molecules apparently suppressed the Au-5*d* orbitals to the lower position in 4H phase of 4H/fcc Au-OAm (Figure 4f). As a comparison, the fcc phase shows a slight upshifting from bulk to the surface. These results suggest that the coverage of OAm molecules decreases the Au surface electroactivity for the CO_2RR process. Moreover, the broad peak of Au-5*d* orbitals also leads to the low selectivity of the 4H/fcc Au-OAm. Therefore, the different electronic structures of 4H/fcc Au-MMT and 4H/fcc Au-OAm indicate that surface ligands play a critical role in modulating the electroactivity.

Besides the electronic structure, the reaction energies of $HCOO^-$ and CO generation on 4H/fcc Au-MMT and 4H/fcc Au-OAm were also compared (Figure 4g, h). For the formation of $HCOO^-$, the 4H/fcc Au-MMT show an energy barrier of 0.11 eV for the initial hydrogenation step, which is much lower than the energy barrier of 0.56 eV on 4H/fcc Au-OAm (Figure 4g). Moreover, the overall reaction trend on 4H/fcc Au-MMT is also stronger than that on 4H/fcc Au-OAm, supporting the higher $HCOO^-$ selectivity of 4H/fcc Au-MMT. For the generation of CO, the

energy barrier for the formation of COOH* on 4H/fcc Au-MMT is significantly reduced compared to that of 4H/fcc Au-OAm (Figure 4h). These results all support the greatly improved electroactivity of 4H/fcc Au-MMT than 4H/fcc Au-OAm for CO_2RR under different potentials. For 4H/fcc Au-MMT, although the energy barrier for the formation of $HCOO^-$ is slightly smaller than that of the CO, the transition levels (TS) of the initial hydrogenation of the CO pathway (0.27 eV) are smaller than that of the HCOOH pathway (0.46 eV), leading to the improved selectivity towards CO formation. Moreover, the reaction energy for CO generation shows overall formation energy of -0.88 eV, which is lower than that of $HCOO^-$ (0.43 eV), supporting the stronger formation trend to CO. At lower potential, the lowered energy barrier leads to the partial formation of $HCOO^-$ while the CO becomes the dominant product at the higher potential.

Besides MMT, we have also investigated several other molecules, which possess a similar chemical structure to MMT, for the surface molecular functionalization of 4H/fcc Au nanorods towards electrochemical CO_2RR (**Figure 5**). As shown in Figure 5a, four kinds of MMT derivatives, including 5-mercapto-1-phenyl-1*H*-tetrazole (MPT), 3-mercapto-4-methyl-4*H*-1,2,4-triazole (MCMT), 3-mercapto-1,2,4-triazole (MCT) and 3-methyl-1*H*-1,2,4-triazole-5-thiol (MTT), were used to modify the surface of 4H/fcc Au nanorods via ligand exchange (see "Methods" for details). The successful surface molecular functionalization of 4H/fcc Au nanorods with MPT, MCMT, MCT and MTT was identified by FT-IR measurements (Figures S14-S17). The LSV plots reveal that 4H/fcc Au-MPT and 4H/fcc Au-MCMT show almost equal current density, while 4H/fcc Au-MCT and 4H/fcc Au-MTT exhibit higher current density, compared to 4H/fcc Au-OAm (Figure 5b). Importantly, these four Au catalysts all show much enhanced FE_{CO} than 4H/fcc Au-OAm under a wide potential window of −0.5 V to −0.9 V (vs RHE, Figure 5c). As a result, they all display much larger geometric J_{CO} than 4H/fcc Au-OAm in a broad potential range (Figure 5d). In addition, similar to 4H/fcc Au-MMT, $HCOO^-$ is also one of the main products at −0.4 V (vs RHE) for these four Au catalysts (Figure S18). Under

more negative potentials, the FE of $HCOO^-$ decreases sharply to below 5%. These results reveal that surface molecular functionalization of 4H/fcc Au nanorods with a family of MMT derivatives can also significantly improve the CO_2RR performance.

In order to further explore the universality of this surface molecular functionalization method, we also tried to modify the surface of conventional phase (i.e., fcc) Au nanostructures with MMT for CO_2RR. Specifically, high-purity fcc Au nanourchins capped with OAm (denoted as fcc Au-OAm) were synthesized with a wet-chemical method (see "Methods" for details, Figures S19-S21). After surface molecular functionalization of fcc Au nanourchins with MMT, both morphology and crystal phase are well maintained, leading to the formation of fcc Au nanourchins capped with MMT (denoted as fcc Au-MMT, Figures S22-S24). Subsequently, the CO_2RR performance of fcc Au-OAm and fcc Au-MMT was measured in H-type cell (Figure S25). The LSV plots indicate that fcc Au-MMT exhibits a much higher current density than the fcc Au-OAm (Figure S25a). For both fcc Au catalysts, CO is the main CO_2-reduction product, together with the generation of $HCOO^-$ at low potentials, as shown in Figure S25b, d and e. Importantly, the fcc Au-MMT exhibit much higher FE_{CO} than the fcc Au-OAm in the potential range of −0.4 V to −0.6 V (vs RHE), while both fcc Au catalysts show comparable FE_{CO} in the more negative potential window (Figure S25b). As a result, the fcc Au-MMT delivers a much larger geometric J_{CO} than fcc Au-OAm under the whole operating potential window (Figure 25c). Remarkably, the geometric J_{CO} of fcc Au-MMT is more than two times that of fcc Au-OAm in the potential range of −0.4 V to −0.6 V (vs RHE). These results suggest that surface molecular functionalization of fcc Au nanourchins with MMT can also significantly enhance the CO_2RR performance.

3. Conclusion

In summary, a facile surface molecular functionalization strategy has been successfully

developed to boost the electrochemical CO_2RR performance of unusual phase metal nanomaterials under industry-relevant current density. The obtained 4H/fcc Au-MMT demonstrated greatly enhanced CO_2RR performance in H-type cell over a wide range of applied potentials compared to the original 4H/fcc Au-OAm. Significant improvement of CO selectivity was achieved in the flow cell through surface molecular functionalization of 4H/fcc Au nanorods with MMT, especially at the industry-relevant current density. DFT calculations have unraveled the converse modulation effect by OAm and MMT ligands on 4H/fcc Au nanorods. The surface MMT activates the surface Au in both fcc and 4H phases for an efficient CO_2RR process with low reaction barriers. In comparison, surface OAm not only suppresses the electroactivity but also induces spatial barriers for intermediate adsorptions. In addition, surface molecular functionalization of 4H/fcc Au nanorods with a family of MMT derivatives can also remarkably increase the CO_2RR performance. And this facile surface molecular functionalization method has also been extended to the conventional fcc Au nanomaterials in improving CO_2RR performance. It is believed that the rational surface modification could provide an effective approach to enhance the CO_2RR performance of metal nanomaterials towards practical applications.

Supporting Information
Supporting Information is available from the Wiley Online Library or from the author.

Acknowledgement
J. Wang, J. Yu, M. Sun and L. Liao contributed equally to this work. This work was supported by ITC via Hong Kong Branch of National Precious Metals Material Engineering Research Center (NPMM), and Grants (Project No. 9610480, 7005512, 7005600 and 9680301) from City University of Hong Kong, and Start-Up Grant (Project No. 4930977) from The Chinese University of Hong Kong, and Grants (Project No. 22005258, 22175148, 21771156 and 52025025) from National Natural Science Foundation of China.

Conflict of Interest
The authors declare no competing financial interest.

Received: ((will be filled in by the editorial staff))
Revised: ((will be filled in by the editorial staff))
Published online: ((will be filled in by the editorial staff))

References

1. De Luna, P.; Hahn, C.; Higgins, D.; Jaffer, S. A.; Jaramillo, T. F.; Sargent, E. H., *Science* **2019,** *364*, eaav3506.

2. Chen, C.; Khosrowabadi Kotyk, J. F.; Sheehan, S. W., *Chem* **2018,** *4*, 2571-2586.

3. Nitopi, S.; Bertheussen, E.; Scott, S. B.; Liu, X.; Engstfeld, A. K.; Horch, S.; Seger, B.; Stephens, I. E. L.; Chan, K.; Hahn, C.; Norskov, J. K.; Jaramillo, T. F.; Chorkendorff, I., *Chem. Rev.* **2019,** *119*, 7610-7672.

4. Jiang, X.; Nie, X.; Guo, X.; Song, C.; Chen, J. G., *Chem. Rev.* **2020,** *120*, 7984-8034.

5. Ross, M. B.; De Luna, P.; Li, Y.; Dinh, C.-T.; Kim, D.; Yang, P.; Sargent, E. H., *Nat. Catal.* **2019,** *2*, 648-658.

6. Sa, Y. J.; Lee, C. W.; Lee, S. Y.; Na, J.; Lee, U.; Hwang, Y. J., *Chem. Soc. Rev.* **2020,** *49*, 6632-6665.

7. Zou, Y.; Wang, S., *Adv. Sci.* **2021**, 2003579.

8. Franco, F.; Rettenmaier, C.; Jeon, H. S.; Roldan Cuenya, B., *Chem. Soc. Rev.* **2020,** *49*, 6884-6946.

9. Morales-Guio, C. G.; Cave, E. R.; Nitopi, S. A.; Feaster, J. T.; Wang, L.; Kuhl, K. P.; Jackson, A.; Johnson, N. C.; Abram, D. N.; Hatsukade, T.; Hahn, C.; Jaramillo, T. F., *Nat. Catal.* **2018,** *1*, 764-771.

10. Kuhn, A. N.; Zhao, H.; Nwabara, U. O.; Lu, X.; Liu, M.; Pan, Y. T.; Zhu, W.; Kenis, P. J. A.; Yang, H., *Adv. Funct. Mater.* **2021,** *31*, 2101668.

11. Wang, Z.; Yang, G.; Zhang, Z.; Jin, M.; Yin, Y., *ACS Nano* **2016,** *10*, 4559-64.

12. De Gregorio, G. L.; Burdyny, T.; Loiudice, A.; Iyengar, P.; Smith, W. A.; Buonsanti, R., *ACS Catal.* **2020,** *10*, 4854-4862.

13. Mariano, R. G.; McKelvey, K.; White, H. S.; Kanan, M. W., *Science* **2017,** *358*, 1187-1192.

14. Wang, Y. F.; Han, P.; Lv, X. M.; Zhang, L. J.; Zheng, G. F., *Joule* **2018,** *2*, 2551-2582.

15. Zhang, B.; Zhang, J.; Hua, M.; Wan, Q.; Su, Z.; Tan, X.; Liu, L.; Zhang, F.; Chen, G.; Tan, D.; Cheng, X.; Han, B.; Zheng, L.; Mo, G., *J. Am. Chem. Soc.* **2020,** *142*, 13606-13613.

16. Zhuang, T.-T.; Liang, Z.-Q.; Seifitokaldani, A.; Li, Y.; De Luna, P.; Burdyny, T.; Che, F.; Meng, F.; Min, Y.; Quintero-Bermudez, R.; Dinh, C. T.; Pang, Y.; Zhong, M.; Zhang, B.; Li, J.; Chen, P.-N.; Zheng, X.-L.; Liang, H.; Ge, W.-N.; Ye, B.-J.; Sinton, D.; Yu, S.-H.; Sargent, E. H., *Nat. Catal.* **2018,** *1*, 421-428.

17. Xia, Z.; Guo, S., *Chem. Soc. Rev.* **2019,** *48*, 3265-3278.

18. Ma, S.; Sadakiyo, M.; Heima, M.; Luo, R.; Haasch, R. T.; Gold, J. I.; Yamauchi, M.; Kenis, P. J., *J. Am. Chem. Soc.* **2017,** *139*, 47-50.

19. Fan, Z.; Bosman, M.; Huang, Z.; Chen, Y.; Ling, C.; Wu, L.; Akimov, Y. A.; Laskowski, R.; Chen, B.; Ercius, P.; Zhang, J.; Qi, X.; Goh, M. H.; Ge, Y.; Zhang, Z.; Niu, W.; Wang, J.; Zheng, H.; Zhang, H., *Nat. Commun.* **2020,** *11*, 3293.

20. Lu, S.; Liang, J.; Long, H.; Li, H.; Zhou, X.; He, Z.; Chen, Y.; Sun, H.; Fan, Z.; Zhang, H., *Acc. Chem. Res.* **2020,** *53*, 2106-2118.

21. Chen, Y.; Fan, Z.; Wang, J.; Ling, C.; Niu, W.; Huang, Z.; Liu, G.; Chen, B.; Lai, Z.; Liu, X.; Li, B.; Zong, Y.; Gu, L.; Wang, J.; Wang, X.; Zhang, H., *J. Am. Chem. Soc.* **2020,** *142*, 12760-12766.

22. Li, H. X.; Zhou, X. C.; Zhai, W.; Lu, S. Y.; Liang, J. Z.; He, Z.; Long, H. W.; Xiong, T. F.; Sun, H. Y.; He, Q. Y.; Fan, Z. X.; Zhang, H., *Adv Energy Mater* **2020,** *10*, 2002019.

23. Wang, P.; Qiao, M.; Shao, Q.; Pi, Y.; Zhu, X.; Li, Y.; Huang, X., *Nat. Commun.* **2018,** *9*, 4933.

24. Yu, J. L.; Wang, J.; Ma, Y. B.; Zhou, J. W.; Wang, Y. H.; Lu, P. Y.; Yin, J. W.; Ye, R. Q.; Zhu, Z. L.; Fan, Z. X., *Adv. Funct. Mater.* **2021,** *31*, 2102151.

25. Zheng, T.; Jiang, K.; Wang, H., *Adv. Mater.* **2018,** *30*, 1802066.

26. Jin, S.; Hao, Z.; Zhang, K.; Yan, Z.; Chen, J., *Angew. Chem. Int. Ed.* **2021,** *60*, 2-24.

27. Mezzavilla, S.; Horch, S.; Stephens, I. E. L.; Seger, B.; Chorkendorff, I., *Angew. Chem. Int. Ed.* **2019,** *58*, 3774-3778.

28. Shi, R.; Guo, J.; Zhang, X.; Waterhouse, G. I. N.; Han, Z.; Zhao, Y.; Shang, L.; Zhou, C.; Jiang, L.; Zhang, T., *Nat. Commun.* **2020,** *11*, 3028.

29. Rogers, C.; Perkins, W. S.; Veber, G.; Williams, T. E.; Cloke, R. R.; Fischer, F. R., *J. Am. Chem. Soc.* **2017,** *139*, 4052-4061.

30. Li, S.; Nagarajan, A. V.; Alfonso, D. R.; Sun, M.; Kauffman, D. R.; Mpourmpakis, G.; Jin, R., *Angew. Chem. Int. Ed.* **2021,** *60*, 6351-6356.

31. Liu, S.; Tao, H.; Zeng, L.; Liu, Q.; Xu, Z.; Liu, Q.; Luo, J. L., *J. Am. Chem. Soc.* **2017,** *139*, 2160-2163.

32. Ma, M.; Liu, K.; Shen, J.; Kas, R.; Smith, W. A., *ACS Energy Lett.* **2018,** *3*, 1301-1306.

33. Zhang, N.; Zhang, X.; Tao, L.; Jiang, P.; Ye, C.; Lin, R.; Huang, Z.; Li, A.; Pang, D.; Yan, H.; Wang, Y.; Xu, P.; An, S.; Zhang, Q.; Liu, L.; Du, S.; Han, X.; Wang, D.; Li, Y., *Angew. Chem. Int. Ed.* **2021,** *60*, 6170-6176.

34. Ma, Y.; Wang, J.; Yu, J.; Zhou, J.; Zhou, X.; Li, H.; He, Z.; Long, H.; Wang, Y.; Lu, P.; Yin, J.; Sun, H.; Zhang, Z.; Fan, Z., *Matter* **2021,** *4*, 888-926.

35. Nam, D. H.; De Luna, P.; Rosas-Hernandez, A.; Thevenon, A.; Li, F.; Agapie, T.; Peters, J. C.; Shekhah, O.; Eddaoudi, M.; Sargent, E. H., *Nat. Mater.* **2020,** *19*, 266-276.

36. Cao, Z.; Derrick, J. S.; Xu, J.; Gao, R.; Gong, M.; Nichols, E. M.; Smith, P. T.; Liu, X.; Wen, X.; Coperet, C.; Chang, C. J., *Angew. Chem. Int. Ed.* **2018,** *57*, 4981-4985.

37. Zhang, L.; Wei, Z.; Thanneeru, S.; Meng, M.; Kruzyk, M.; Ung, G.; Liu, B.; He, J., *Angew. Chem. Int. Ed.* **2019,** *58*, 15834-15840.

38. Zhou, Y.; Che, F.; Liu, M.; Zou, C.; Liang, Z.; De Luna, P.; Yuan, H.; Li, J.; Wang, Z.; Xie, H.; Li, H.; Chen, P.; Bladt, E.; Quintero-Bermudez, R.; Sham, T. K.; Bals, S.; Hofkens, J.; Sinton, D.; Chen, G.; Sargent, E. H., *Nat. Chem.* **2018,** *10*, 974-980.

39. Scholten, F.; Sinev, I.; Bernal, M.; Roldan Cuenya, B., *ACS Catal.* **2019,** *9*, 5496-5502.

40. Narouz, M. R.; Osten, K. M.; Unsworth, P. J.; Man, R. W. Y.; Salorinne, K.; Takano, S.; Tomihara, R.; Kaappa, S.; Malola, S.; Dinh, C. T.; Padmos, J. D.; Ayoo, K.; Garrett, P. J.; Nambo, M.; Horton, J. H.; Sargent, E. H.; Hakkinen, H.; Tsukuda, T.; Crudden, C. M., *Nat. Chem.* **2019,** *11*, 419-425.

41. Mistry, H.; Varela, A. S.; Bonifacio, C. S.; Zegkinoglou, I.; Sinev, I.; Choi, Y. W.; Kisslinger, K.; Stach, E. A.; Yang, J. C.; Strasser, P.; Cuenya, B. R., *Nat. Commun.* **2016,** *7*, 12123.

42. Jiang, K.; Huang, Y. F.; Zeng, G. S.; Toma, F. M.; Goddard, W. A.; Bell, A. T., *Acs Energy Lett.* **2020,** *5*, 1206-1214.

43. Mistry, H.; Choi, Y. W.; Bagger, A.; Scholten, F.; Bonifacio, C. S.; Sinev, I.; Divins, N. J.; Zegkinoglou, I.; Jeon, H. S.; Kisslinger, K.; Stach, E. A.; Yang, J. C.; Rossmeisl, J.; Roldan Cuenya, B., *Angew. Chem. Int. Ed.* **2017,** *56*, 11394-11398.

44. Cao, Z.; Zacate, S. B.; Sun, X.; Liu, J.; Hale, E. M.; Carson, W. P.; Tyndall, S. B.; Xu, J.; Liu, X.; Liu, X.; Song, C.; Luo, J. H.; Cheng, M. J.; Wen, X.; Liu, W., *Angew. Chem. Int. Ed.* **2018,** *57*, 12675-12679.

45. Wakerley, D.; Lamaison, S.; Ozanam, F.; Menguy, N.; Mercier, D.; Marcus, P.; Fontecave, M.; Mougel, V., *Nat. Mater.* **2019,** *18*, 1222-1227.

46. Xie, M. S.; Xia, B. Y.; Li, Y.; Yan, Y.; Yang, Y.; Sun, Q.; Chan, S. H.; Fisher, A.; Wang, X., *Energy Environ. Sci.* **2016,** *9*, 1687-1695.

47. Li, F.; Li, Y. C.; Wang, Z.; Li, J.; Nam, D.-H.; Lum, Y.; Luo, M.; Wang, X.; Ozden, A.; Hung, S.-F.; Chen, B.; Wang, Y.; Wicks, J.; Xu, Y.; Li, Y.; Gabardo, C. M.; Dinh, C.-T.; Wang, Y.; Zhuang, T.-T.; Sinton, D.; Sargent, E. H., *Nat. Catal.* **2019,** *3*, 75-82.

48. Li, F.; Thevenon, A.; Rosas-Hernandez, A.; Wang, Z.; Li, Y.; Gabardo, C. M.; Ozden, A.; Dinh, C. T.; Li, J.; Wang, Y.; Edwards, J. P.; Xu, Y.; McCallum, C.; Tao, L.; Liang, Z. Q.; Luo, M.; Wang, X.; Li, H.; O'Brien, C. P.; Tan, C. S.; Nam, D. H.; Quintero-Bermudez, R.; Zhuang, T. T.; Li, Y. C.; Han, Z.; Britt, R. D.; Sinton, D.; Agapie, T.; Peters, J. C.; Sargent, E.

H., *Nature* **2020,** *577*, 509-513.

49. Zhong, S.; Yang, X.; Cao, Z.; Dong, X.; Kozlov, S. M.; Falivene, L.; Huang, J. K.; Zhou, X.; Hedhili, M. N.; Lai, Z.; Huang, K. W.; Han, Y.; Cavallo, L.; Li, L. J., *Chem. Commun.* **2018,** *54*, 11324-11327.

50. Cao, Z.; Kim, D.; Hong, D.; Yu, Y.; Xu, J.; Lin, S.; Wen, X.; Nichols, E. M.; Jeong, K.; Reimer, J. A.; Yang, P.; Chang, C. J., *J. Am. Chem. Soc.* **2016,** *138*, 8120-8125.

51. Jiang, B.; Zhang, X. G.; Jiang, K.; Wu, D. Y.; Cai, W. B., *J. Am. Chem. Soc.* **2018,** *140*, 2880-2889.

52. Kim, C.; Eom, T.; Jee, M. S.; Jung, H.; Kim, H.; Min, B. K.; Hwang, Y. J., *ACS Catal.* **2016,** *7*, 779-785.

53. Lau, G. P.; Schreier, M.; Vasilyev, D.; Scopelliti, R.; Gratzel, M.; Dyson, P. J., *J. Am. Chem. Soc.* **2016,** *138*, 7820-7823.

54. Chen, Y.; Lai, Z.; Zhang, X.; Fan, Z.; He, Q.; Tan, C.; Zhang, H., *Nat. Rev. Chem.* **2020,** *4*, 243-256.

55. Fan, Z.; Huang, X.; Chen, Y.; Huang, W.; Zhang, H., *Nat. Protoc.* **2017,** *12*, 2367-2378.

56. Fan, Z.; Zhang, H., *Chem. Soc. Rev.* **2016,** *45*, 63-82.

57. Fan, Z.; Zhang, H., *Acc. Chem. Res.* **2016,** *49*, 2841-2850.

58. Fan, Z.; Bosman, M.; Huang, X.; Huang, D.; Yu, Y.; Ong, K. P.; Akimov, Y. A.; Wu, L.; Li, B.; Wu, J.; Huang, Y.; Liu, Q.; Png, C. E.; Gan, C. L.; Yang, P.; Zhang, H., *Nat. Commun.* **2015,** *6*, 7684.

59. Jia, L.; Sun, M.; Xu, J.; Zhao, X.; Zhou, R.; Pan, B.; Wang, L.; Han, N.; Huang, B.; Li, Y., *Angew. Chem.. Int. Ed.* **2021,** *60*, 21741-21745.

60. Tan, X.; Geng, S.; Ji, Y.; Shao, Q.; Zhu, T.; Wang, P.; Li, Y.; Huang, X., *Adv. Mater.* **2020,** *32*, e2002857.

61. Chen, Y.; Fan, Z.; Luo, Z.; Liu, X.; Lai, Z.; Li, B.; Zong, Y.; Gu, L.; Zhang, H., *Adv. Mater.* **2017,** *29*, 1701331.

62. Fan, Z.; Huang, X.; Han, Y.; Bosman, M.; Wang, Q.; Zhu, Y.; Liu, Q.; Li, B.; Zeng, Z.; Wu, J.; Shi, W.; Li, S.; Gan, C. L.; Zhang, H., *Nat. Commun.* **2015,** *6*, 6571.

63. Cheng, H.; Yang, N.; Liu, G.; Ge, Y.; Huang, J.; Yun, Q.; Du, Y.; Sun, C. J.; Chen, B.; Liu, J.; Zhang, H., *Adv. Mater.* **2020,** *32*, 1902964.

64. El-Sayed, N.; Trouillet, V.; Clasen, A.; Jung, G.; Hollemeyer, K.; Schneider, M., *Adv. Healthcare Mater.* **2019,** *8*, 1900993.

65. Qie, L.; Chen, W.; Xiong, X.; Hu, C.; Zou, F.; Hu, P.; Huang, Y., *Adv. Sci.* **2015,** *2*, 1500195.

66. Qiang, Y.; Li, H.; Lan, X., *J. Mater. Sci. Technol.* **2020,** *52*, 63-71.

67. Wang, N.; Miao, R. K.; Lee, G.; Vomiero, A.; Sinton, D.; Ip, A. H.; Liang, H.; Sargent, E. H., *SmartMat* **2021,** *2*, 12-16.

68. Huang, J. E.; Li, F. W.; Ozden, A.; Rasouli, A. S.; Arquer, F. P. G.; Liu, S. J.; Zhang, S. Z.; Luo, M. C.; Wang, X.; Lum, Y. W.; Xu, Y.; Bertens, K.; Miao, R. K.; Dinh, C. T.; Sinton, D.; Sargent, E. H., *Science* **2021,** *372*, 1074-1078.

69. Niu, Z. Z.; Chi, L. P.; Liu, R.; Chen, Z.; Gao, M. R., *Energy Environ. Sci.* **2021,** *14*, 4169-4176.

70. Qi, Z.; Biener, M. M.; Kashi, A. R.; Hunegnaw, S.; Leung, A.; Ma, S.; Huo, Z.; Kuhl, K. P.; Biener, J., *Mater. Res. Lett.* **2020,** *9*, 99-104.

71. Jhong, H. M.; Tornow, C. E.; Kim, C.; Verma, S.; Oberst, J. L.; Anderson, P. S.; Gewirth, A. A.; Fujigaya, T.; Nakashima, N.; Kenis, P. J. A., *ChemPhysChem* **2017,** *18*, 3274-3279.

72. Seong, H.; Efremov, V.; Park, G.; Kim, H.; Yoo, J. S.; Lee, D., *Angew. Chem. Int. Ed.* **2021,** *60*, 14563-14570.

73. Verma, S.; Hamasaki, Y.; Kim, C.; Huang, W.; Lu, S.; Jhong, H.-R. M.; Gewirth, A. A.; Fujigaya, T.; Nakashima, N.; Kenis, P. J. A., *ACS Energy Lett.* **2017,** *3*, 193-198.

Figures

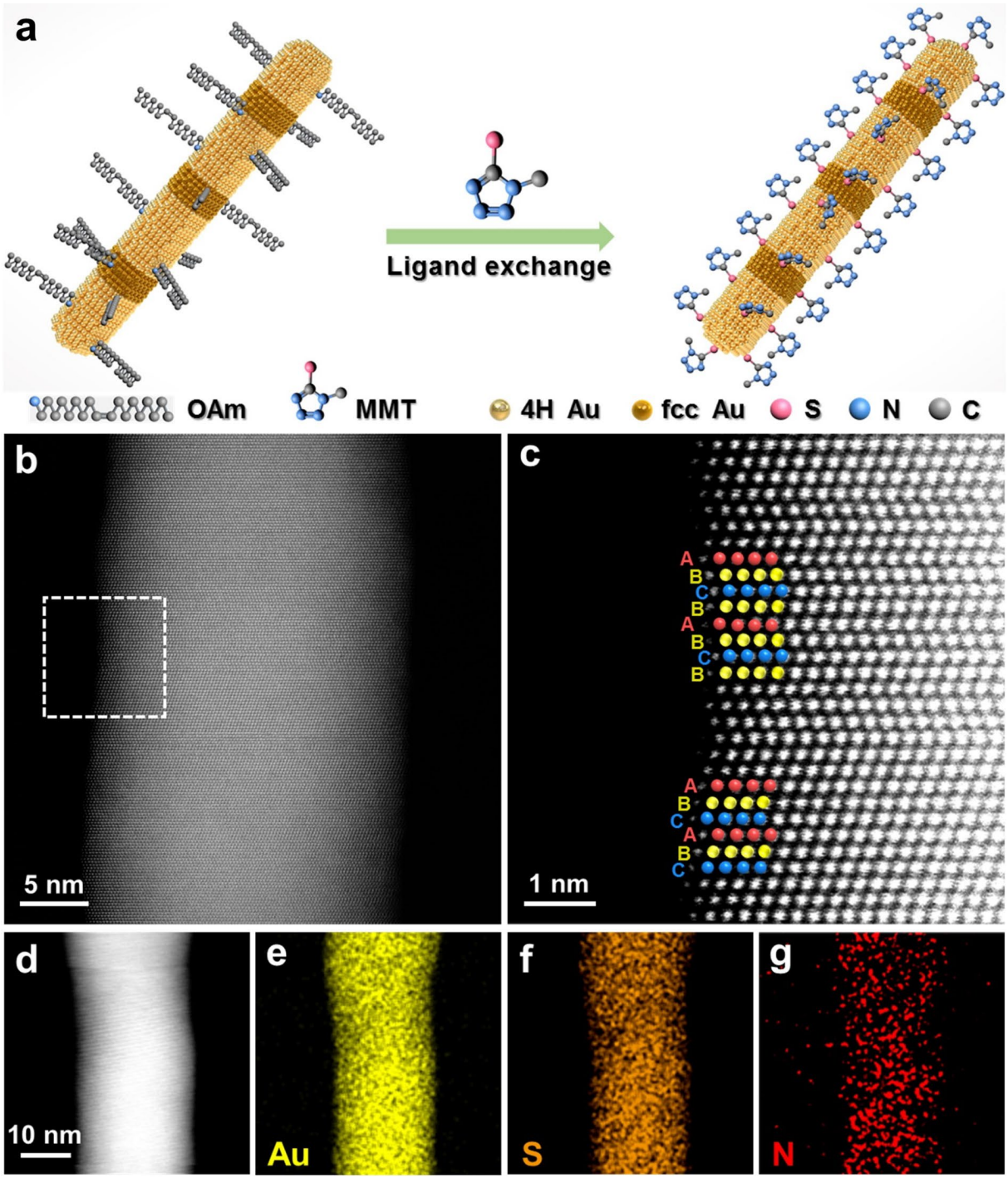

Figure 1. Preparation and STEM characterization of 4H/fcc Au-MMT. (a) Schematic illustration for the surface molecular functionalization of 4H/fcc Au nanorods via ligand exchange between OAm and MMT. All hydrogen atoms in the chemical structure of OAm and MMT molecules are omitted for clarity. (b) Aberration-corrected HAADF-STEM image of 4H/fcc Au-MMT. (c) Zoom-in HAADF-STEM image taken from the corresponding square region in (b). (d-g) STEM image (d) and the corresponding STEM–EDS elemental mappings (e-g) of 4H/fcc Au-MMT.

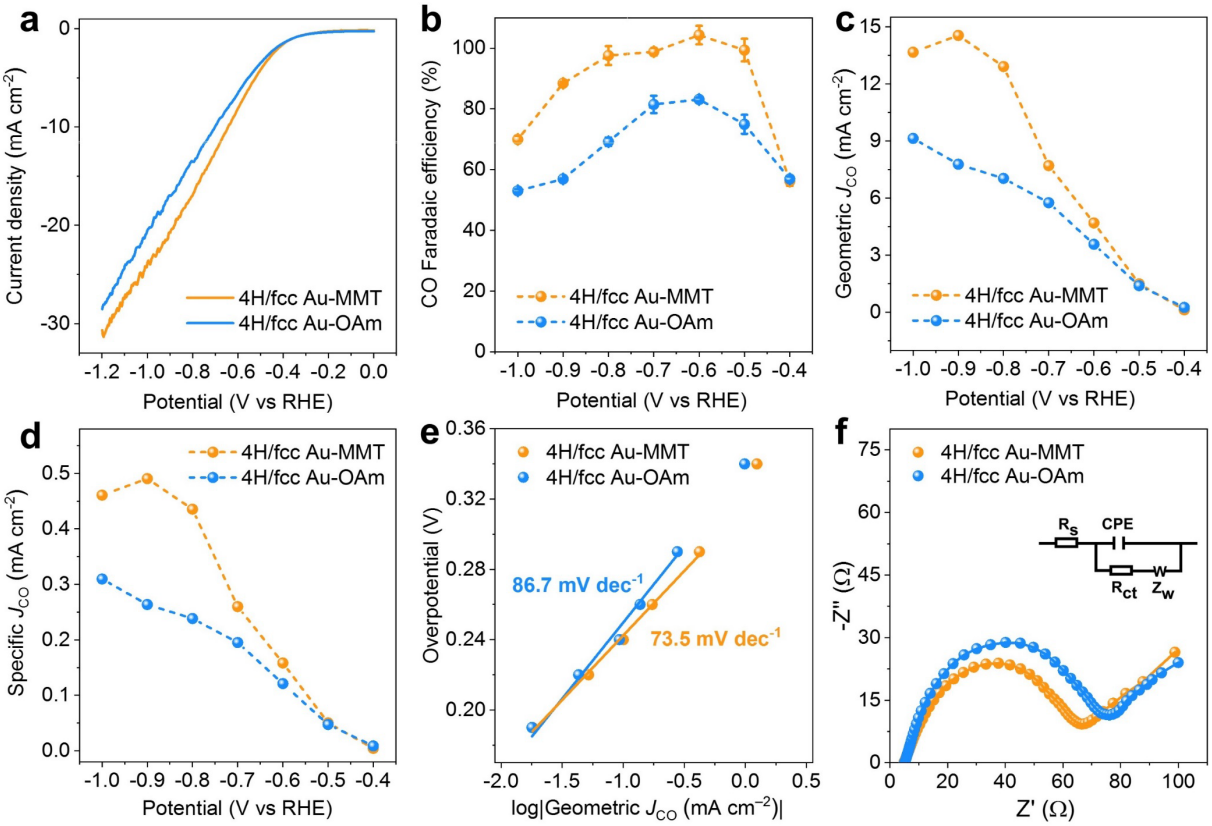

Figure 2. Electrocatalytic performance of 4H/fcc Au-MMT and 4H/fcc Au-OAm towards CO_2RR in H-type cell. (a) LSV plots of 4H/fcc Au-MMT and 4H/fcc Au-OAm in CO_2-saturated 0.5 M $KHCO_3$ aqueous solution. (b-d) FE_{CO} (b), geometric J_{CO} (c), and specific J_{CO} (d) of 4H/fcc Au-MMT and 4H/fcc Au-OAm under different potentials. (e, f) Tafel plots (e) and Nyquist plots of the electrochemical impedance spectra (f) of 4H/fcc Au-MMT and 4H/fcc Au-OAm. Inset of (f): schematic illustration of the Randles equivalent circuit used to fit electrochemical impedance spectra. R_s, electrolyte resistance; CPE, constant phase angle element; R_{ct}, charge transfer resistance; Z_w, Warburg impedance.

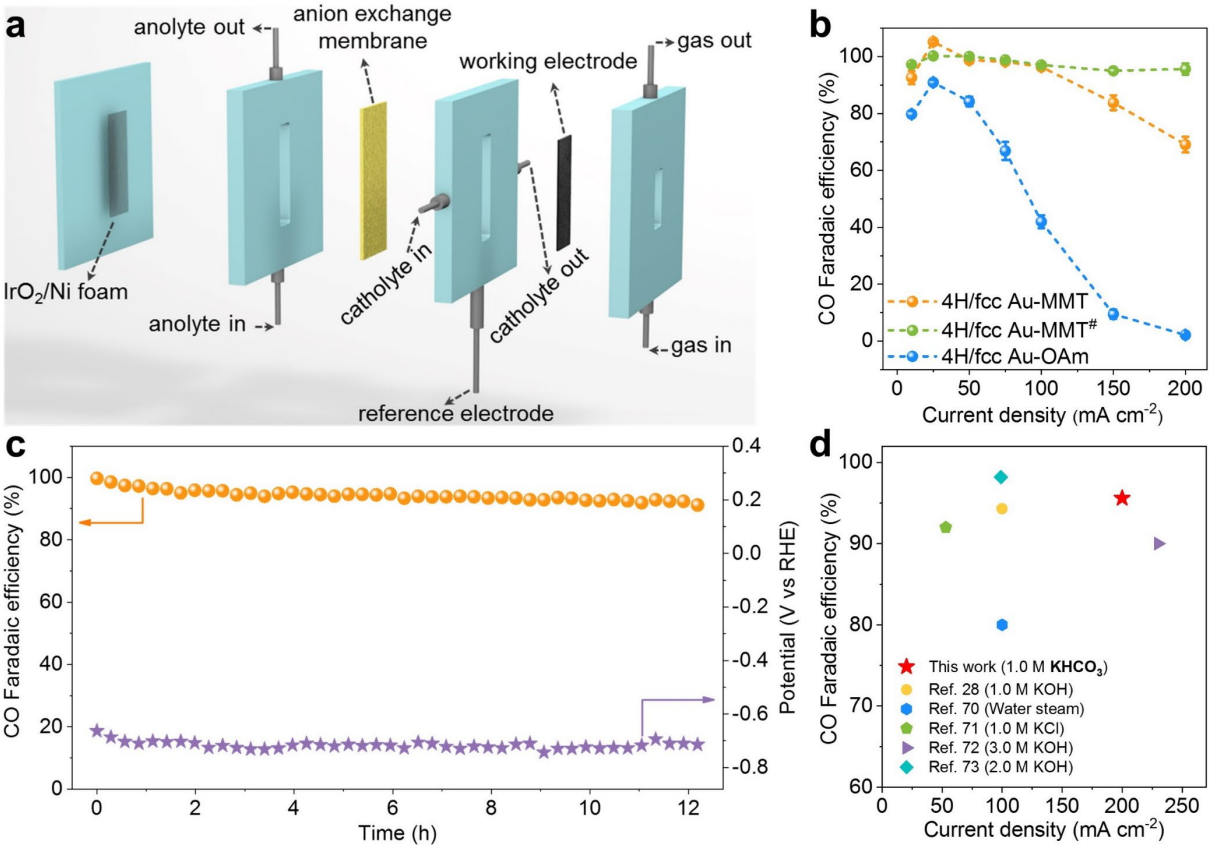

Figure 3. Electrocatalytic performance of 4H/fcc Au-MMT and 4H/fcc Au-OAm towards CO_2RR in flow cell. (a) Schematic illustration of the flow cell. (b) FE_{CO} of 4H/fcc Au-MMT and 4H/fcc Au-OAm in CO_2-saturated 1.0 M $KHCO_3$ aqueous solution under different current densities. [#]The loading amount of Au in this sample is 400 μg. (c) Long-term durability test of 4H/fcc Au-MMT at 50 mA cm^{-2}. (d) Comparison of the CO_2RR performance of 4H/fcc Au-MMT with reported Au electrocatalysts. The catholytes are also listed for comparison.

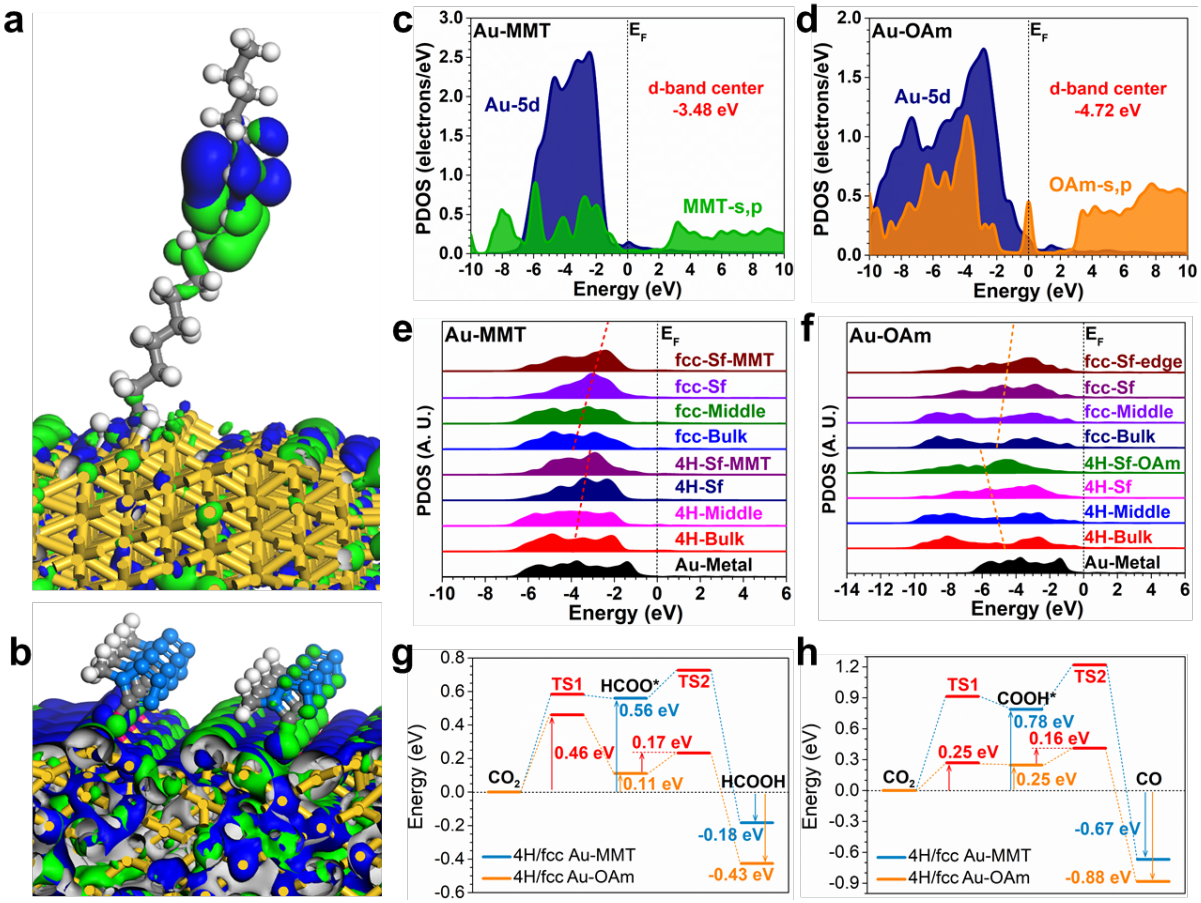

Figure 4. Theoretical calculations for the electrocatalytic CO_2RR on 4H/fcc Au-MMT and 4H/fcc Au-OAm. (a, b) The 3D contour plots of electronic distribution near Fermi level of (a) 4H/fcc Au-OAm and (b) 4H/fcc Au-MMT. Yellow, grey, light blue, pink and white balls represent Au, C, N, S and H atoms, respectively. Blue and green isosurfaces refer to the bonding orbitals and anti-bonding orbitals, respectively. (c, d) The PDOS of (c) 4H/fcc Au-MMT and (d) 4H/fcc Au-OAm. (e, f) The site-dependent PDOS of Au-5*d* in (e) 4H/fcc Au-MMT and (f) 4H/fcc Au-OAm. (g, h) The comparison of reaction trend for the conversion of CO_2 to (g) $HCOO^-$ and (h) CO on 4H/fcc Au-MMT and 4H/fcc Au-OAm.

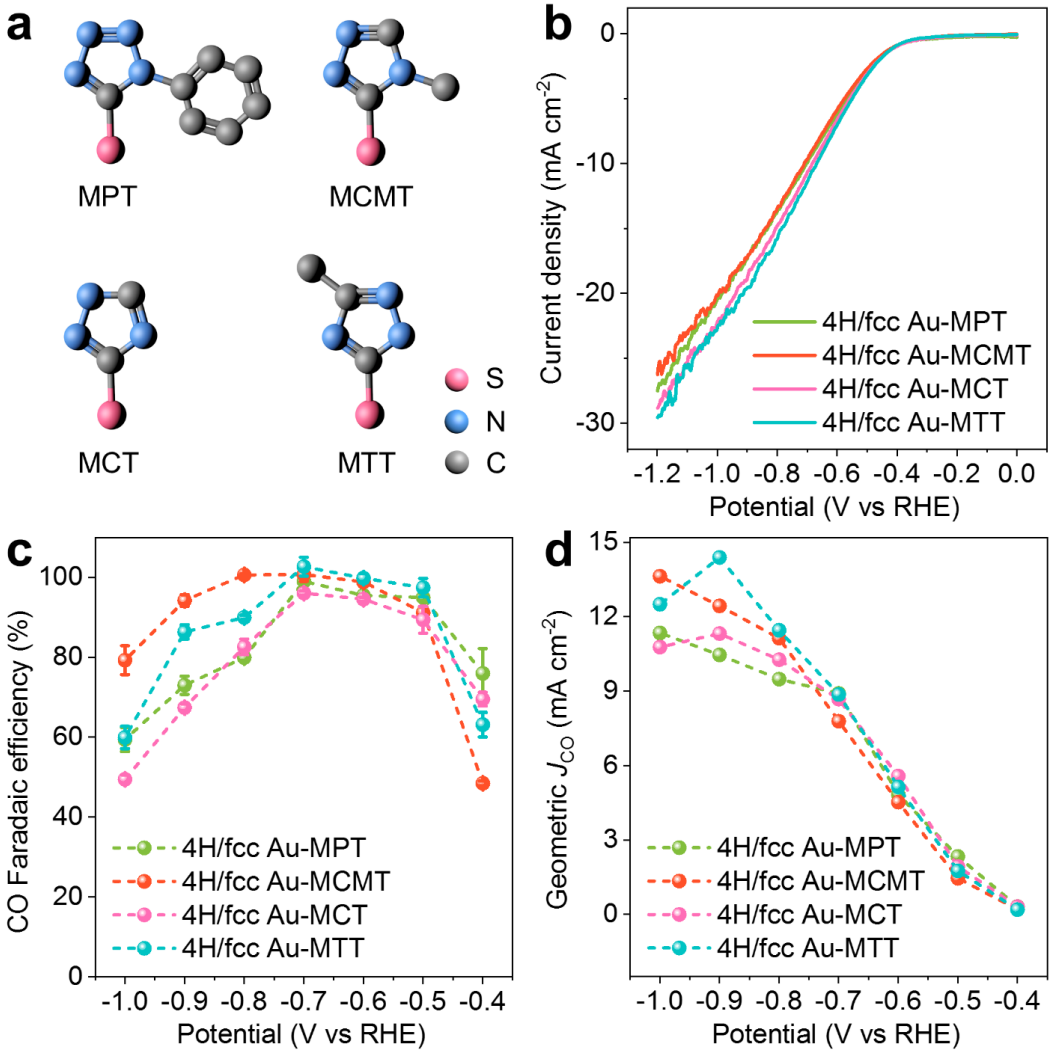

Figure 5. Electrocatalytic performance of 4H/fcc Au nanorods capped with various MMT derivatives towards CO_2RR in H-type cell. (a) Chemical structures of MPT, MCMT, MCT and MTT. All hydrogen atoms are omitted for clarity. (b) LSV plots of 4H/fcc Au nanorods modified with MPT, MCMT, MCT and MTT in CO_2-saturated 0.5 M $KHCO_3$ aqueous solution. (c, d) FE_{CO} (c) and geometric J_{CO} (d) of 4H/fcc Au nanorods modified with MPT, MCMT, MCT and MTT under different potentials.

Surface molecular functionalization of unusual phase Au nanorods with 5-mercapto-1-methyltetrazole (MMT) significantly enhances the electrochemical CO_2 reduction reaction (CO_2RR) performance in both H-type cell and flow cell, especially under industry-relevant current density of 200 mA cm^{-2}, comparing to original Au nanorods. This facile surface molecular functionalization strategy is also applicable to various MMT derivatives as well as conventional Au nanostructures in boosting CO_2RR performance.

J. Wang, J. Yu, M. Sun, L. Liao, Q. Zhang, L. Zhai, X. Zhou, L. Li, G. Wang, F. Meng, D. Shen, Z. Li, H. Bao, Y. Wang, J. Zhou, Y. Chen, W. Niu, B. Huang,* L. Gu,* C.-S. Lee and Z. Fan*

Surface Molecular Functionalization of Unusual Phase Metal Nanomaterials for Highly Efficient Electrochemical Carbon Dioxide Reduction under Industry-Relevant Current Density

TOC figure